



## Article

# Investigation of Morphology of Aluminum Co-Doped Scandium Stabilized Zirconia (ScAlSZ) Thin Films

Arvidas Galdikas , Mantas Sriubas , Gediminas Kairaitis, Darius Virbukas, Kristina Bockute, Matas Galdikas, Teresa Moskaliuviene and Giedrius Laukaitis

Physics Department, Kaunas University of Technology, Studentu Str. 50, LT-51368 Kaunas, Lithuania; mantas.sriubas@ktu.lt (M.S.); gediminas.kairaitis@ktu.lt (G.K.); darius.virbukas@ktu.lt (D.V.); kristina.bockute@ktu.lt (K.B.); matas.galdikas@ktu.lt (M.G.); teresa.moskaliuviene@ktu.lt (T.M.); giedrius.laukaitis@ktu.lt (G.L.)

\* Correspondence: arvidas.galdikas@ktu.lt

**Abstract:** The morphology of aluminum co-doped scandium stabilized zirconia (ScAlSZ) thin films formed by e-beam deposition system was investigated experimentally and theoretically. The dependencies of surface roughness, and the films' structure on deposition temperature and deposition rate were analyzed. It was shown experimentally that the dependence of the surface roughness on deposition temperature and deposition rate was not monotonic. Those dependencies were analyzed by mathematical modeling. The mathematical model includes the processes of phase separation, adsorption and diffusion process due to the film surface curvature. The impacts of substrate temperature, growth rate on surface roughness of thin films and lateral nanoparticle sizes are shown by the modeling results. Modeling showed that the roughness of the surface of grown films became higher in most cases as the substrate's temperature rose, but the higher deposition rate resulted in lower surface roughness in most cases. The results obtained by simulations were compared to the relevant experimental data. The non-linear relationships between surface roughness of grown films and lateral size of nanoparticles were also shown by our modeling results, which suggested that the variation in the surface roughness depending on the substrate temperature and growth rate was related to the lateral size of nanoparticles.

**Keywords:** aluminum co-doped scandium stabilized zirconia; phase separation; kinetic modeling; thin films; surface roughness; compounds



**Citation:** Galdikas, A.; Sriubas, M.; Kairaitis, G.; Virbukas, D.; Bockute, K.; Galdikas, M.; Moskaliuviene, T.; Laukaitis, G. Investigation of Morphology of Aluminum Co-Doped Scandium Stabilized Zirconia (ScAlSZ) Thin Films. *Coatings* **2022**, *12*, 31. <https://doi.org/10.3390/coatings12010031>

Academic Editor: Panos Pouloupoulos

Received: 18 November 2021

Accepted: 23 December 2021

Published: 27 December 2021

**Publisher's Note:** MDPI stays neutral with regard to jurisdictional claims in published maps and institutional affiliations.



**Copyright:** © 2021 by the authors. Licensee MDPI, Basel, Switzerland. This article is an open access article distributed under the terms and conditions of the Creative Commons Attribution (CC BY) license (<https://creativecommons.org/licenses/by/4.0/>).

## 1. Introduction

High ionic conductivity (0.1–0.01 S/cm) [1] is one of the reasons to consider zirconium oxide-based ceramic thin films as the electrolyte for solid oxide fuel cells (SOFC). High ionic conductivity of zirconium oxide is achieved by doping or co-doping it as dopants and co-dopants stabilize the structure and create vacancies of oxygen ions. On the other hand, the microstructure of thin films has a great effect on ionic conductivity as well. Roughness of the surface is expected to influence charge transfer at the electrolyte/electrode interface, which would impact the electrochemical impedance of SOFCs. [2]. Grain and grain boundary conductivities strongly decrease with increasing porosity [3,4]. Moreover, it is generally agreed that grain boundaries act as barriers to oxygen ion diffusion [5,6]. According to the brick layer model, the electrical grain boundary consists of core and two space charge layers whose thickness is equal to the Debye length [7]. Oxygen vacancies are severely depleted in the space charge layers [5], and dopant concentration increases [6], therefore, diffusion of oxygen ions does not occur along grain boundaries [8,9] and ionic conductivity decreases with increasing density of grain boundaries and the ratio of space charge layer to the grain area. It follows that ionic conductivity depends on the shape of grains and their size [10,11].

Zirconium oxide-based thin films tend to have a columnar structure. The result of such growth is a high density of grain boundaries and dislocations. So far, there has been little agreement on the influence of columnar growth on ionic conductivity. Data from several studies [12,13] suggest that columnar grain boundaries act as barriers for oxygen diffusion, and columnar grain boundaries act as rapid diffusion paths. Contrary to the previously published studies, T. Kiguchi et al. demonstrated that total ionic conductivity was restricted by the columnar growth, and columnar structure with high coherence was preferred [14,15].

To obtain the highest ionic conductivity, the microstructure of zirconium oxide-based ceramic thin films must be carefully controllable. Different formation methods, e.g., e-beam evaporation, and the chosen formation parameters allow us to achieve it. E-beam evaporation is suitable for the formation of ceramic thin films due to the possibility of heating the material to 3000–4000 °C temperatures. Such high temperatures permit the attainment and control of deposition rates between 0.02 nm/s to 10 nm/s. In addition, the obtained thin films' structure is not dependent on the structure of evaporating material as ZrO<sub>2</sub> evaporates by partial decomposition [16,17]. The vapor phase consists of ZrO<sub>2</sub>, ZrO, O<sub>2</sub>, or O atoms, molecules, and molecule fragments.

The growth of thin film begins when the atoms, molecules, and molecule fragments evaporated from the vapor phase reach the surface of the substrate. This complex process involves the formation of nucleation centers followed by island growth, coalescence of islands, formation of polycrystalline islands and channels, development of continuous structure, and thickness growth [18–21]. The most important stage is nucleation. An adatom that arrives on the surface usually has non-zero mobility and can diffuse onto the surface. Diffusion of an adatom occurs until it finds and joins an existing island or meets another adatom. The dimmer or nucleus dissociates if other adatoms do not arrive at a certain time, i.e., the nucleus does not reach a critical size [22]. The diffusion distance decreases with increasing number of islands and finally becomes constant [23]. At this moment nucleation of new islands is prevented and all adatoms join existing islands. The number of islands ( $N$ ) is dependent on deposition rate ( $F$ ) and diffusion coefficient ( $D$ )  $N = F/D$  [24,25]. The number of islands is higher if the deposition rate is higher and lower if diffusion distance is higher (substrate temperature and arrived particle energy). Moreover, the growth of thin films after the nucleation phase strongly depends on the ratio of substrate temperature ( $T_s$ ) to the melting temperature of thin-film material ( $T_m$ ),  $T_s/T_m$  [26]. If  $T_s/T_m < 0.2$  (Zone I), the surface diffusion is negligible. Consequently, thin films consist of small randomly-oriented grains that develop during the nucleation and growth stages. The grains grow with the same rate independently of their orientation and form fibrous structure [27]. If  $0.2 < T_s/T_m < 0.4$  (Zone T), the surface diffusion predominates and competitive growth occurs [19,28]. At lower temperatures, the mobility of adatoms which are close to grain boundaries is low and, therefore, they presumably become incorporated at a low diffusivity surface compared to adatoms at high diffusivity planes. This results in a faster growth of the grains with low surface diffusivities, e.g., (001) [18]. However, at higher temperatures island coalescence starts to occur due to the increased surface diffusion and grain boundary motion [29]. During the coalescence process, the densest planes of the grains, e.g., (111) result in the formation of face-centered cubic [19] structure. Grains have a V shape and roughness with temperature increases. At higher temperatures, when  $T_s/T_m > 0.4$  (Zone II), surface and bulk diffusion becomes significant. Therefore, grain boundary migration occurs not only during coalescence but through the chickening process also, and the large textured grains dominate in the zone II [18].

The phase structure influences many properties of a nanocomposite material [10,11,30–33] and it is crucial to comprehend the influence of various growth variables such as substrate temperature, deposition rate, contents of depositing particles, etc. It may lead to a better development of the desired structures of composites and help explain the mechanism causing the formation of a particular phase structure. In addition, surface roughness is also influenced by many electrochemical, optical, and mechanical properties of nanocompos-

ites [34] together with deposition parameters such as temperature of the substrate during the deposition, deposition rate, composition of the evaporated powder, the substrate's surface pretreatment, etc. The physical processes that occur during the growth of the thin film affect the surface roughness [23], hence the understanding of the relationship between this characteristic and the particular growth conditions is a valuable source to better comprehend the growth mechanisms and may allow better control of desired properties of composites.

There have been several recent works dealing with the simulation of the growth of nanostructured thin films [35–43]. The influence of deposition rate and substrate temperature on the phase structure of the Cu-Mo films was examined using the approaches based on the phase-field models by Derby et al. [35] and Ankit et al. [36]. By using the kinetic Monte Carlo approaches, the effects of substrate tilt angle [37], substrate temperature [38], deposition rate [13,14], and composition [39] on the phase structure of nanocomposites have been recently investigated. Bouaouina et al. in [37] discovered that the surface roughness and the phase structure of TiN thin films are influenced by the change of substrate tilt angle: an increase in the substrate tilt angle caused an increase in the tilt angle of TiN columns and the surface roughness as well. The factors affecting the stress generation in metallic thin films with body-centered cubic lattice structure were examined by using a molecular dynamics approach [40] by Zhou et al. and Stewart and Dingreville [41] and showed the influence of deposition rate, phase fraction, and the dissimilar elastic response on thin films growth during simulated physical vapor deposition. Powers et al. [42] were focused on determining the kinetic conditions favorable to the development of hierarchical phase structures during a thin film growth (in immiscible alloy systems: Cu-Ta, Cu-Fe, Cu-Mo, Cu-Ag, Mo-Ag, Cu-Mo-Ag). Our previous work [42] examined the influence of substrate temperature and relative incoming ion flux on the phase structure and surface roughness of grown films. A model based on the phase-field approach was used in [43]. The modeling results [43] showed that both substrate temperature and incoming ion flux influenced the surface roughness of grown film and the average nanoparticle size.

The aim of this study was to examine the impact of the simulation parameters on the formation of the thin films and their microstructure. Moreover, by using a mathematical model, the work contributes to the analysis of the influence of substrate temperature and growth rate on the surface roughness and phase structure of compound thin films. The mathematical model involves the Cahn–Hilliard equation to simulate the phase separation process of film growth that takes place. The processes of adsorption and diffusion due to surface curvature (of a growing film) are also included in the model. The dependencies of surface roughness on temperature and growth rate are analyzed. The relationships between surface roughness of grown films and average nanoparticle size are reported. The findings are compared to the experimental data dealing with aluminum co-doped scandium stabilized zirconia thin films formed using an e-beam deposition method.

## 2. Materials and Methods

### 2.1. Experimental

Aluminum co-doped scandium stabilized zirconia (ScAlSZ) thin films (~1500 nm) were formed using an e-beam physical vapor deposition system (Kurt J. Lesker EB-PVD 75, Kurt J. Lesker Company Ltd., Hastings, UK). The pellets of pressed  $(\text{Sc}_2\text{O}_3)_{0.10}(\text{Al}_2\text{O}_3)_{0.01}(\text{ZrO}_2)_{0.89}$  powders were used as evaporating material. The formation was carried out on amorphous  $\text{SiO}_2$  using 0.2, 0.4, 0.8, 1.2 and 1.6 nm/s deposition rates and 20, 150, 300, 450 or 600 °C substrate temperatures. Prior to the deposition, the substrates were cleaned in an ultrasonic bath and processed in  $\text{Ar}^+$  ion plasma for 10 min. The deposition rate was monitored with an INFICON (Inficon, Bad Ragaz, Switzerland) crystal sensor and adjusted by changing the e-beam current in a range of 60–100 mA. The electron gun's accelerating voltage was kept constant, i.e., 7.9 kV. The pressure was  $\sim 2.0 \times 10^{-2}$  Pa in the vacuum chamber during the deposition process. The rotation speed of the substrates was kept at 8 rpm.

The elemental analysis was performed using energy-dispersive X-ray spectroscopy (EDS) (BrukerXFlash QUAD 5040, Bruker AXS GmbH, Karlsruhe, Germany). The accelerating voltage of 15 kV, 6 min. sampling time, and  $1000\times$  magnification were used. Sc, Al, Zr, and O concentrations can be found in Supplementary Materials (Table S1). A scanning electron microscope (SEM) (Hitachi S-3400N, Hitachi High-Technologies Corporation, Tokyo, Japan) was used to obtain cross-section images. Images were obtained using secondary electron mode and 5 kV accelerating voltage. The atomic force microscope (AFM) (NT-206, Microtestmachines Co., Gomel, Belarus) was used to obtain topographic images ( $10\ \mu\text{m} \times 10\ \mu\text{m}$ ) of ScAlSZ thin films. The tapping mode with 20 nm step size was chosen for AFM measurements. The Si tip used during the scans was pyramidal shape, 16  $\mu\text{m}$  high, and 6 nm diameter. The samples were measured in three different places each. The surface roughness ( $R_q$ ) was calculated from topographic images using Gwyddion software, and the average values of  $R_q$  were plotted.

## 2.2. Kinetic Model

To model the evolution of concentrations of film components in time and the growth process of a thin film, a three-dimensional grid was used. Three local relative concentrations  $c_A^{i,j,k}$ ,  $c_B^{i,j,k}$ , and  $c_S^{i,j,k}$ , with  $i = 1, \dots, I$ ,  $j = 1, \dots, J$ , and  $k = 1, \dots, K$ , were assigned to each grid point  $i$ ,  $j$ , and  $k$ . They denoted the component concentrations A, B and substrate material, respectively. The indices  $i$  and  $j$  indicated the positions in the horizontal plane directions,  $k$  being the position in the vertical direction toward the film growth direction. The condition  $c_A^{i,j,k} + c_B^{i,j,k} + c_S^{i,j,k} \leq 1$  was always satisfied at any grid cell. The previously published model [43] was used to simulate the growth of thin films. The processes of phase separation, diffusion of both thin components due to surface curvature, and adsorption were included in the model. The phase separation of components was described by the Cahn–Hilliard equations:

$$\frac{\partial c_{A_S}}{\partial t} = \nabla D_A \nabla \left( \frac{df(c_{A_S})}{dc_{A_S}} - \gamma \nabla^2 c_{A_S} \right), \quad (1)$$

where  $c_{A_S}$  ( $c_{A_S}^{i,j}$ ,  $i = 1, \dots, I$ ,  $j = 1, \dots, J$ ) is the concentration of component A on the surface of substrate,  $f$  is the density of free energy (the form of function  $f$  is used the same as in our previous work [29]),  $\gamma$  is a phase gradient power coefficient, and  $D_A$  is a diffusion coefficient.

The parameter  $c_{A_S}^{i,j}$ , which is the concentration variable used in Equation (1), was defined through Equation (2) given in [43]. The changes in component B concentration due to phase separation in the surface layer were also described by Equation (1), but, in order to do this, the term  $c_{A_S}$  in Equation (1) had to be replaced with  $c_{B_S}$  (the concentration of component B in the surface layer), which was defined analogously to Equation (2) given in [43].

We next introduce a new process, which is mathematically described by the Cahn–Hilliard equation given in Equation (1) but with a different concentration variable being used. This new process ensured that atoms of the given type migrating on a nano-island formed of the same type atoms can gather together. This process also influenced the surface patterns of the nano-islands. The new variable  $c_{A_S}^{i,j}$  (see Equation (3) in [43]) (instead of  $c_{A_S}$  defined by Equation (2) in [43]) and the diffusion coefficient  $D_{1A}$  (instead of  $D_A$ ) were used in Equation (1) to get the mathematical description for the considered process. Therefore, the use of Equation (1) with the variable given by Equation (3) in [43] introduced another process that ensured that atoms of type A migrating on a nano-island made of the same type of atoms gather to form or influence the surface pattern. The value  $D_{1A} = D_A$  was used for nano-islands made of component A, and  $D_{1A} = 0$  was used anywhere else. An identical process was defined for component B by the types of equations given in Equations (1) and (3) found in [43], but the respective variable that represented

the concentration of component B (instead of the concentration of component A) was used to get the description of the process for component B.

Atomic diffusion on the nano-island surface initiated by its surface curvature was also included in the model by the following equation:

$$\frac{\partial c_{A-S}}{\partial t} = \nabla D_A \nabla \left( -p_A c_{A-S} \nabla^2 h \right), \quad (2)$$

The term  $\nabla^2 h$  denoted the surface curvature,  $h$  was the position parameter, and  $p_A$  was the coefficient of proportionality. Equation (2) ensured that atoms diffuse from crests to valleys on the surface of nano-islands due to their surface curvature. Equation (2) was also used to define the changes in component B, but  $c_{B-S}$  and  $p_B$  had to be used instead of  $c_{A-S}$ , and  $p_A$ , respectively, in Equation (2).

The concentrations changes occurred due to the process of adsorption were described by the following expressions:

$$\begin{aligned} \frac{\partial c_{A-S}^{i,j,k*}}{\partial t} &= k_{AA} i_A c_{A-S}^{i,j} + k_{AB} i_A c_{B-S}^{i,j} + k_{AS} i_A c_{S-S}^{i,j}, \\ \frac{\partial c_{B-S}^{i,j,k*}}{\partial t} &= k_{BA} i_B c_{A-S}^{i,j} + k_{BB} i_B c_{B-S}^{i,j} + k_{BS} i_B c_{S-S}^{i,j}, \end{aligned} \quad (3)$$

$I = 1, \dots, I$ ,  $j = 1, \dots, J$ , and  $k_{AA}$ ,  $k_{AB}$ , and  $k_{AS}$ , are the sticking coefficients,  $i_A$  and  $i_B$  are relative fluxes, and  $c_{A-S}^{i,j}$ ,  $c_{B-S}^{i,j}$ , and  $c_{S-S}^{i,j}$  are the surface concentrations.

Equations (1)–(3), describing the different processes with respect to the thin film component, were added together to get the final model for that component. Since we investigated two growing phases, two models consisting of Equations (1)–(3) concerning each growing phase were considered. To analyze a large temperature range, the diffusion was discriminated into the three regimes: (1) thermal diffusion ( $D_{Th}$ ), (2) radiation enhanced diffusion ( $D_{Rad}$ ), and (3) ion beam mixing ( $D_m$ ). Assuming this, the dependence of the diffusion coefficient  $D_A$  on the substrate temperature  $T$  was expressed as follows:

$$D_A = \begin{cases} D_m = \alpha i, & T < 0.2T_m, \\ D_{Rad} = i\beta e^{-\frac{Q_1}{RT}}, & 0.2T_m < T < 0.6T_m \\ D_{Th} = \delta e^{-\frac{Q_2}{RT}}, & T > 0.6T_m \end{cases} \quad (4)$$

where  $I = i_A + i_B$  is the relative total flux of components,  $\alpha$ ,  $\beta$ , and  $\delta$  are the coefficients of proportionality, and  $Q_1$  and  $Q_2$  are the activation energies of radiation enhanced diffusion and thermal diffusion, respectively. In our calculations, the value of melting temperature  $T_m = \sim 3000$  K (value close to the melting temperature of ScAlSZ ceramics) was used.

### 3. Results and Discussion

ScAlSZ thin films have different microstructures depending on the temperature of the substrate (Figure 1). It is visible that two different surface morphologies exist. Thin films consist of small  $\sim 8$  nm height and  $\sim 200$  nm width grains when using 50–300 °C temperature substrates (Figure 1a–c). In contrast, large triangle prism shape grains grow using higher temperature substrates (Figure 1d,e). The height of triangle prism shape grains is  $\sim 20$  nm and  $\sim 30$  nm for thin films deposited on 450 and 600 °C temperature substrates respectively. The lateral dimensions are  $\sim 800$  nm for 450 °C substrates and  $\sim 900$  nm for 600 °C substrates. The growth of small, randomly-oriented grains indicates that the mobility of adatoms on the surface is low at low temperatures. In comparison, at high temperatures, the mobility of adatoms is high enough to occasion predominant grain growth.

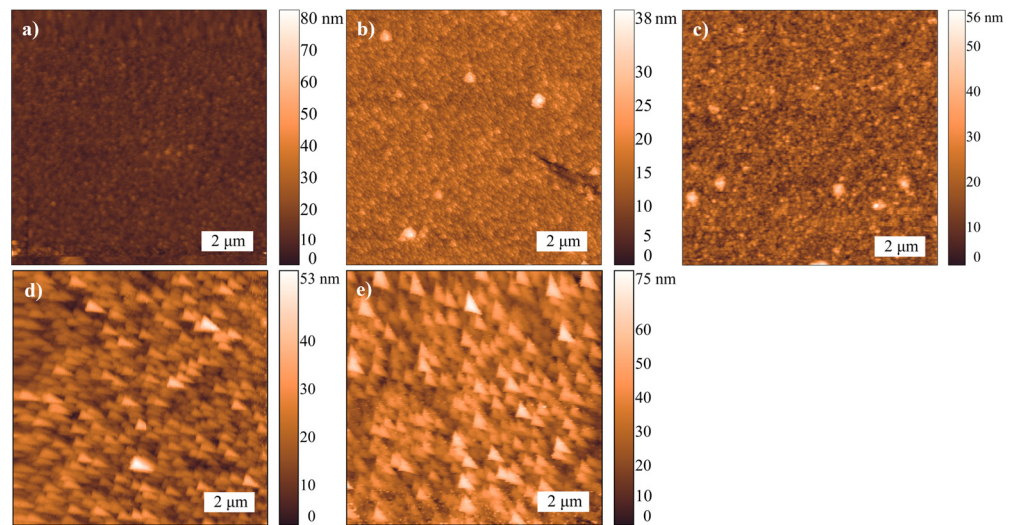


**Figure 1.** AFM topography images of ScAlSZ thin films deposited using a 0.4 nm/s deposition rate and different substrate temperatures: (a) 50 °C, (b) 150 °C, (c) 300 °C, (d) 450 °C, and (e) 600 °C.

The surface roughness calculations indicate that the roughness of ScAlSZ thin films is higher using higher temperature substrates (Figure 2). It increases from 2 to 9.5 nm at 50 and 600 °C substrate temperatures, respectively. There are two values (0.8 and 1.6 nm/s for 600 °C) shifted from the dependence due to the effect of deposition rate. Obtained values of surface roughness are similar to other authors' results [44–46].

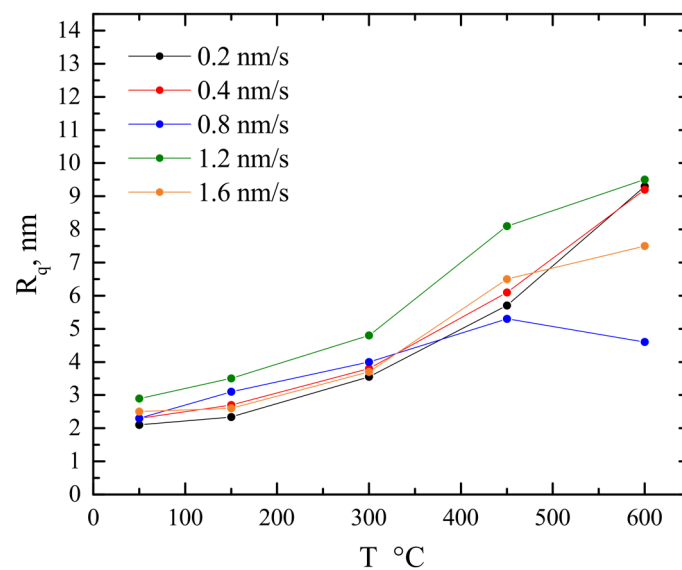


**Figure 2.** Roughness dependence of ScAlSZ thin films on deposition temperature.

The deposition rate affects the growth of ScAlSZ thin films, also (Figure 3). The surface topography is similar for thin films deposited using 0.2, 0.4 and 0.8 nm/s deposition rates (Figure 3a–c). The grains have a triangular prism shape with lateral dimensions of ~600 nm. At higher deposition rates, 1.2 nm/s and 1.6 nm/s (Figure 3d,e), large clusters consisting of few grains form on the surface of thin films. The height of the clusters is ~66 nm and the lateral dimensions ~1700 nm. The clusters of grains started to form due to increased flux of arriving atoms, i.e., the atom flux is high enough to form a new nucleus on the top of grains before the monolayer is finished.

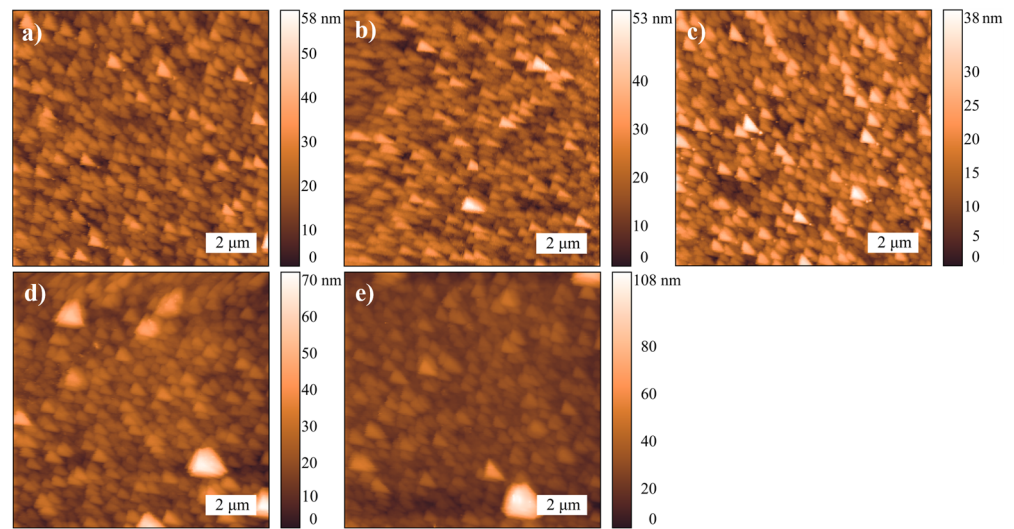


**Figure 3.** AFM topography images of ScAlSZ thin films deposited on 450 °C substrates using different deposition rates: (a) 0.2 nm/s, (b) 0.4 nm/s, (c) 0.8 nm/s, (d) 1.2 nm/s, and (e) 1.6 nm/s.

The dependence of surface roughness on deposition rate is nonlinear at higher deposition temperatures (Figure 4). The peak values of surface roughness are obtained for thin films formed using 0.4 and 1.2 nm/s deposition rates and valley values of the surface roughness are obtained for thin films formed using 0.2, 0.8 and 1.6 nm/s deposition rates. Moreover, our experiments showed that the deposition rate of 1.2 nm/s acts as a breaking point where a sudden decrease of surface roughness appears.

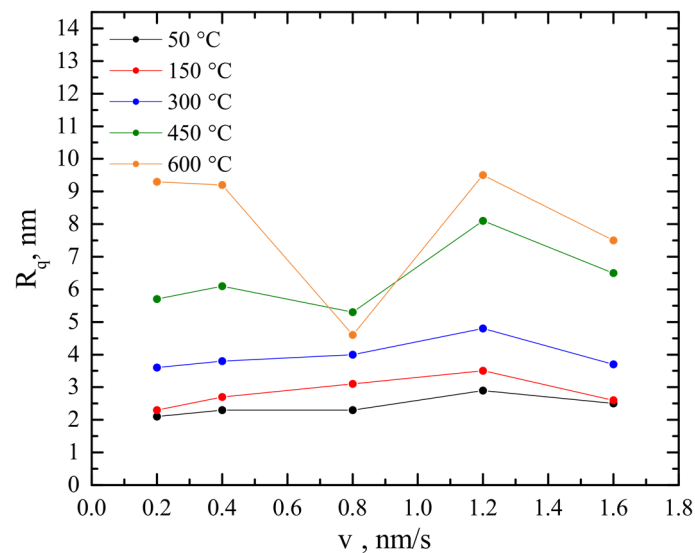


**Figure 4.** Roughness dependence of ScAlSZ thin films on deposition rate at different substrate temperatures during the deposition.

The cross-section photos and XRD results supplement topography images. Thin films are composed of cubic, tetragonal, and rhombohedral phase grains [47]. Small and randomly-oriented grains are visible at low temperatures, e.g., 50 °C (Figure 5a). The columnar structure starts to show up using 300 °C temperature substrates (Figure 5b) and the columns are wider using 600 °C substrates (Figure 5c). At this temperature even prism shape grains are visible (Figure 5c). The deposition rate does not have a visible influence on the growth nature (Figure 6).

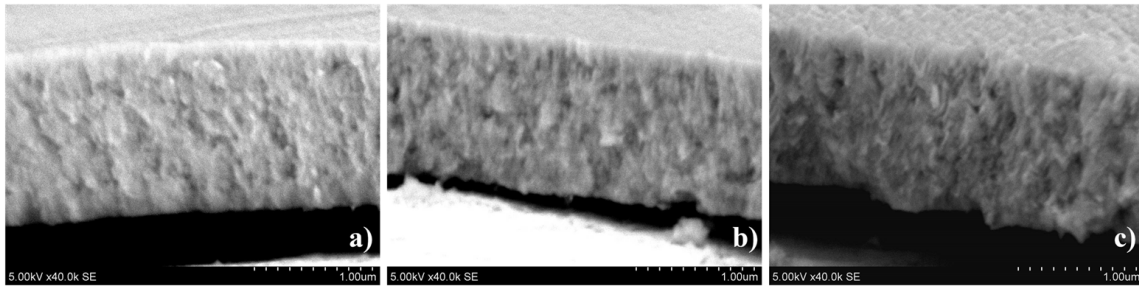


**Figure 5.** Cross-section images of ScAlSZ thin films deposited using 0.4 nm/s deposition rate and different substrate temperatures: (a) 50 °C, (b) 300 °C, and (c) 600 °C.

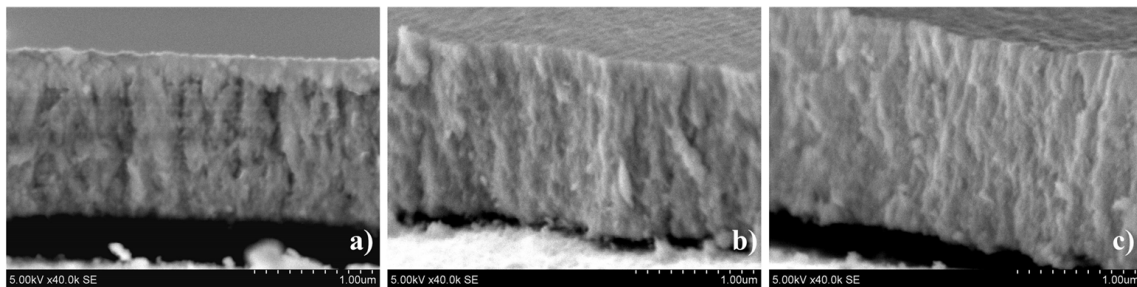


**Figure 6.** Cross-section images of ScAlSZ thin films deposited on 450 °C substrates using different deposition rates: (a) 0.4 nm/s, (b) 0.8 nm/s, and (c) 1.2 nm/s.

The initial conditions assumed a perfectly flat substrate (the lateral dimensions of the substrate are  $36 \text{ nm} \times 36 \text{ nm}$ , the grid spacing is 1 nm) that occupies five computational layers at the beginning of a growth process. On that flat substrate, there is a thin layer made of a random mix of components A and B where concentrations of both components are uniformly distributed in the interval  $\{0, 0.01\}$ . This random thin layer of components A and B lying on top of a perfectly flat substrate is called an initial condition. The concentrations are  $c_A = 30\%$ ,  $c_B = 70\%$ , the values of model parameters  $p_A = p_B = 1.2 \times 10^{-13} \text{ J/m}$  (see Equation (4) in [42]),  $D_B = D_A$  (see Equation (5) and Figure 1 in [43]),  $\gamma = 4.8 \times 10^{-13} \text{ J/m}$  (see Equation (1) in [43]) are assumed for the simulations. The sticking coefficients (see Equation (5) in [43]) are assumed to be equal.

Figure 7 shows the plots of average surface roughness (root mean squared) versus substrate temperature calculated by using the different thin film growth rates. The growth rates of 0.2, 0.4, 0.8, 1.2 and 1.6 nm/s and the substrate temperatures of 50, 200, 350, 500 and 650 °C were used in calculations. Moreover, incoming ion flux also influences the value of the diffusion coefficient. Hence, the dependence of diffusion coefficient on temperature and incoming ion flux is expressed through Equation (4). The values  $2.18 \times 10^{-17}$ ,  $3.18 \times 10^{-17}$ ,  $4.62 \times 10^{-17}$  and  $5.95 \times 10^{-17} \text{ m}^2/\text{s}$  are considered to be the values of the diffusion coefficient at the substrate temperatures of 50, 200, 350, 500 and 650 °C, respectively, at a growth rate of 0.8 nm/s. To get the growth rates of 0.4, 0.8, 1.2 and 1.6 nm/s, the flux values of 0.5, 1.0, 1.5 and  $2.0 \text{ s}^{-1}$  are used, respectively. The diffusion coefficient at the substrate temperatures of 50 and 200 °C is defined as  $D_m$  through Equation (6) in [43]. The diffusion coefficients at the three highest temperatures examined are defined as  $D_{Rad}$  through Equation (6) in [43].



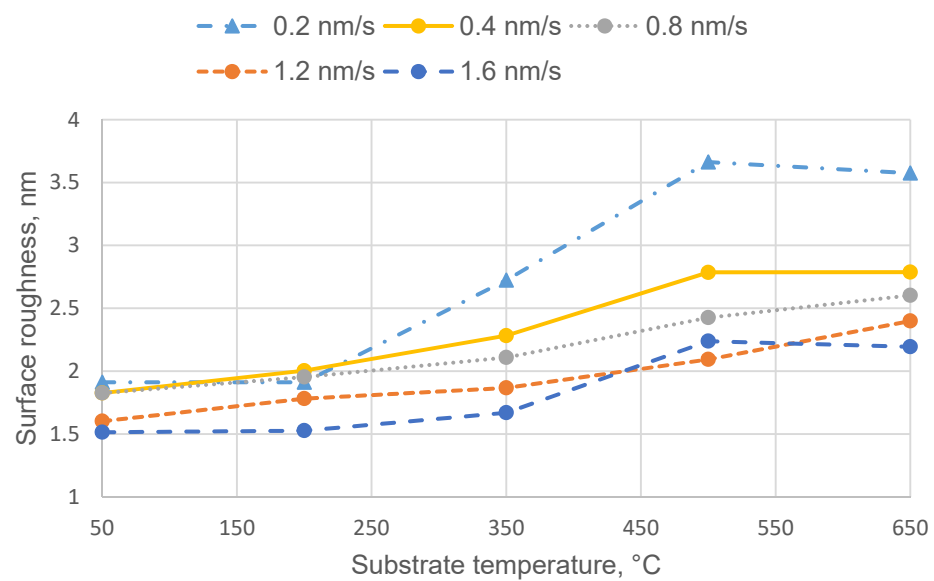


**Figure 7.** Plots of surface roughness versus substrate temperature obtained by using different growth rates.

Each point in Figure 7 is the average result of four different calculations with different initial conditions. It is seen that the average surface roughness increases as the substrate temperature rises in almost all cases examined. Relatively little variation in the surface roughness is observed at the growth rates of 0.2, 0.4 and 1.6 nm/s when the substrate temperature is changed from 500 to 650 °C.

To investigate the reason for the dependence of the surface roughness on the substrate temperature in more detail, a plot of average grain size versus substrate temperature observed at the growth rates of 0.2, 0.4, 0.8, 1.2, and 1.6 nm/s is shown in Figure 8. Figure 8 demonstrates that the average grain sizes monotonically increase as the substrate temperature rises at almost all growth rates presented. The exceptions are observed at the lowest two temperatures investigated (for all growth rates used) and at the lowest growth rate of 0.2 nm/s used when substrate temperature is varied from 500 to 650 °C. Figure 8 reveals that similar monotonic relationships between the substrate temperature and average grain size are observed for all growth rates examined. The curves corresponding to the growth rates of 0.8, 1.2, and 1.6 nm/s are situated very close to each other over the whole temperature range examined, but the curves corresponding to the two lowest growth rates of 0.2 and 0.4 nm/s show some deviations from the curves observed at the three highest growth rates depending on the substrate temperature. Figures 7 and 8 display that both the surface roughness and average grain size are similarly influenced by the increase in the substrate temperature, which suggests that the variation in the thickness of the thin film (it is directly related to the surface roughness) is related to the average grain size. To investigate this relationship in detail, a plot of surface roughness versus average grain size observed at growth rates of 0.2, 0.4, 0.8, 1.2, and 1.6 nm/s is shown in Figure 9, where the surface roughness monotonically increases as the average grain size grows and there is some nonlinear relationship between the surface roughness and the average grain size at growth rates of 0.4, 0.8, and 1.6 nm/s. At a growth rate of 0.2 nm/s a very good linear relationship between the average grain size and the surface roughness with a value of  $R^2$  of 0.9998 (the value and the linear equation are given in Figure 8) is observed. It is found that the surface roughness at the growth rate of 0.4 nm/s varies relatively slowly when the average grain size changes from 7.27 to 10.875 nm and from 11.25 to 14.6 nm, but the variation in the surface roughness is considerably greater when the average grain size changes from 10.875 to 11.25 nm. It is also seen that the variation in the surface roughness at growth rates of 0.8 and 1.6 nm/s shows a similar pattern in comparison to the case with the growth rate of 0.4 nm/s, but the intervals of grain size

values in which the surface roughness varies relatively slowly or quickly are different from the case with the higher growth rate. The given results reveal that the increase in the surface roughness is highly related to the increase in the average lateral grain size. The substrate temperature rises and the value of the diffusion coefficient increases resulting in greater lateral dimensions of grains formed during the phase separation occurring throughout the growth process [48]. The monotonic linear and nonlinear relationships between the average lateral size of grains and the surface roughness are shown by our calculations in Figure 9. This confirms the relationship between the surface roughness and the average grain size in the examined cases.

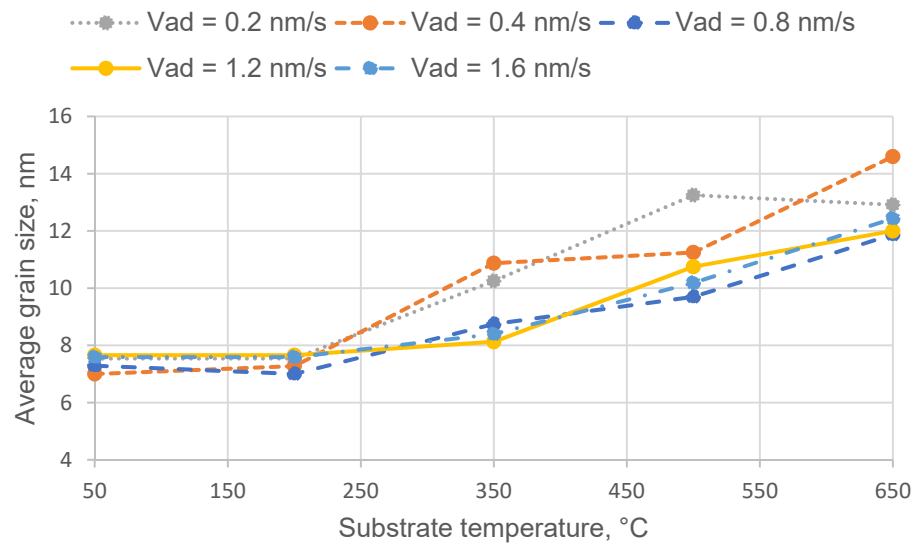


**Figure 8.** Plots of average grain size versus substrate temperature observed at the growth rates of 0.2, 0.4, 0.8, 1.2, and 1.6 nm/s.

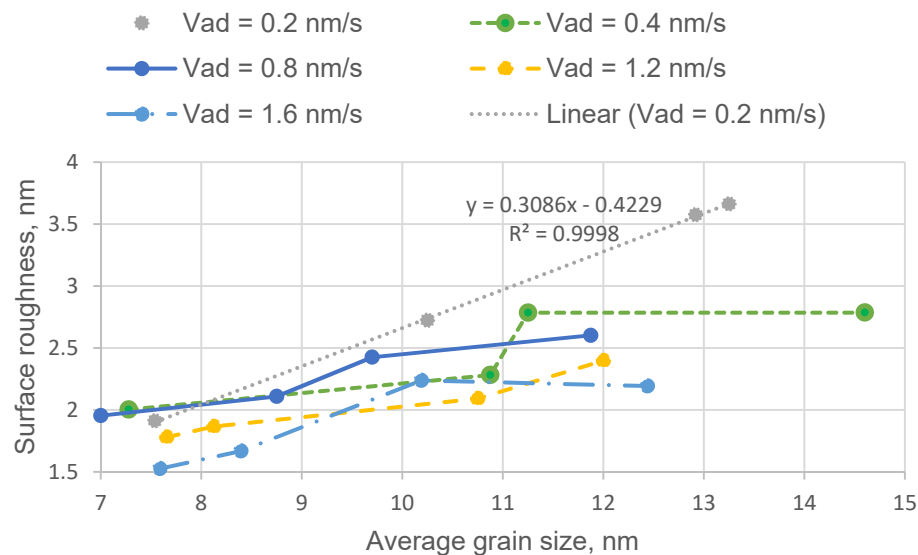


**Figure 9.** Plots of surface roughness versus average grain size observed at the growth rates of 0.2, 0.4, 0.8, 1.2, and 1.6 nm/s.

It is seen from Figure 2 that the surface roughness in ScAlSZ thin films increases with the increase in the substrate temperature at various growth rates in most cases. Similar tendencies are observed in Figure 7, where the influence of substrate temperature on surface roughness determined by modeling is presented. Moreover, the experiments and calculations were performed in the similar range of substrate temperatures. The monotonic

dependencies of the surface roughness on the substrate temperature, showing an increase in the surface roughness with an increase in the substrate temperature, are also observed in YSZ films deposited by pulsed laser deposition [49] and in InN/YSZ films deposited by the reactive RF magnetron sputter deposition technique [50]. Therefore, the qualitative agreement between our modeling results dealing with substrate temperature influence and the mentioned experimental data can be noticed.

Figure 10 provides the cross-sectional views (Figure 10a,d,g) (through the plane  $x = 24$  nm), the concentration plots of component A (Figure 10b,e,h), and the surface maps (Figure 10c,f,i) calculated at the substrate temperatures of 200 °C (Figure 10a–c), 350 °C (Figure 10d–f) and 650 °C 923 K (Figure 10g–i). The used growth rate is 0.8 nm/s. The given surface maps as the two variable functions also represent the thicknesses of the films (with 5 layers of the substrate material included). The areas in Figure 10c,f,i painted in blue mark the regions with a film thickness of 5 nm or the substrate areas not covered with either phase A or B. The areas in Figure 10c,f,i painted in brown indicate the regions where the film thickness is highest. The blue color in Figure 10b,e,h indicates regions which consist of phase B. The brown color in Figure 10b,e,h marks regions of the surface of the thin film, which consists of pure phase A. The cyan color in Figure 10a,d,g indicates regions consisting of phase A, the yellow color marks regions of phase B, and the brown color marks the substrates.

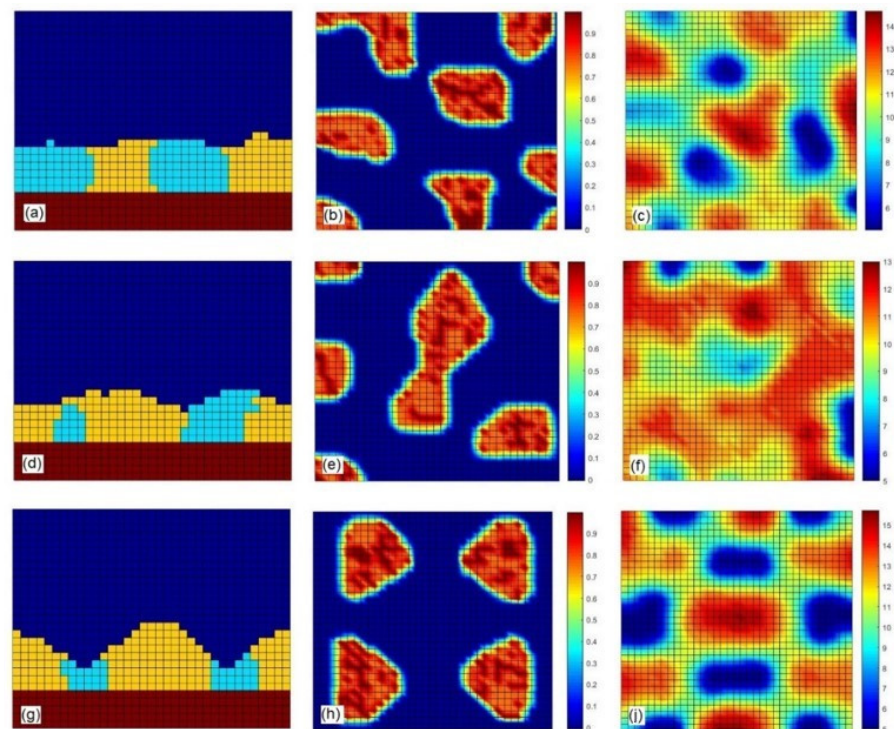


**Figure 10.** Cross-sectional views (a,d,g), concentration plots of component A (in the surface layer of thin films) (b,e,h), and surface maps (c,f,i) calculated at the substrate temperatures of 200 °C (a–c), 350 °C (d–f), and 650 °C (g–i).

It can be seen that, at the lowest given substrate temperature (200 °C), phase 8 A associated individual nanoparticles and a relatively low variation in the film thickness are observed.

As shown in Figure 10d,e the increase in the substrate temperature up to 350 °C causes a higher variation in the film thickness and lowers the number of nanoparticles of component A formed throughout the growth process. At the substrate temperature of 650 °C (see Figure 10g–i) we observe 4 nanoparticles of component A and the highest variation in the film thickness in comparison to the cases corresponding to two lower substrate temperatures. It can also be seen that an increase in the temperature from 200

to 650 °C decreases the number of nanoparticles of phase A from 8 to 4. Since the total concentration of phase A was kept constant in the calculations, the decrease in the number of nanoparticles of phase A increases the average lateral dimensions of nanoparticles of phase A, therefore the results given in Figure 10 also supports the previously-found relationship between the average lateral dimensions of nanoparticles and the surface roughness.

The plots given in Figures 7 and 11 are based on the same calculation data. The plots of surface roughness versus growth rate obtained at the substrate temperatures of 50, 200, 350, 500 and 650 °C indicate that the surface roughness decreases as the film growth rate rises in most cases (Figure 11). The monotonic decrease in the surface roughness is observed at the substrate temperatures of 50, 350, and 650 °C. At the substrate temperature of 500 °C, the surface roughness decreases when the growth rate is changed from 0.2 nm/s to 1.2 nm/s, but there is an increase in the surface roughness when the growth rate is changed from 1.2 nm/s to 1.6 nm/s. This inconsistency should be attributed to the random initial conditions and the limited computational grid size.

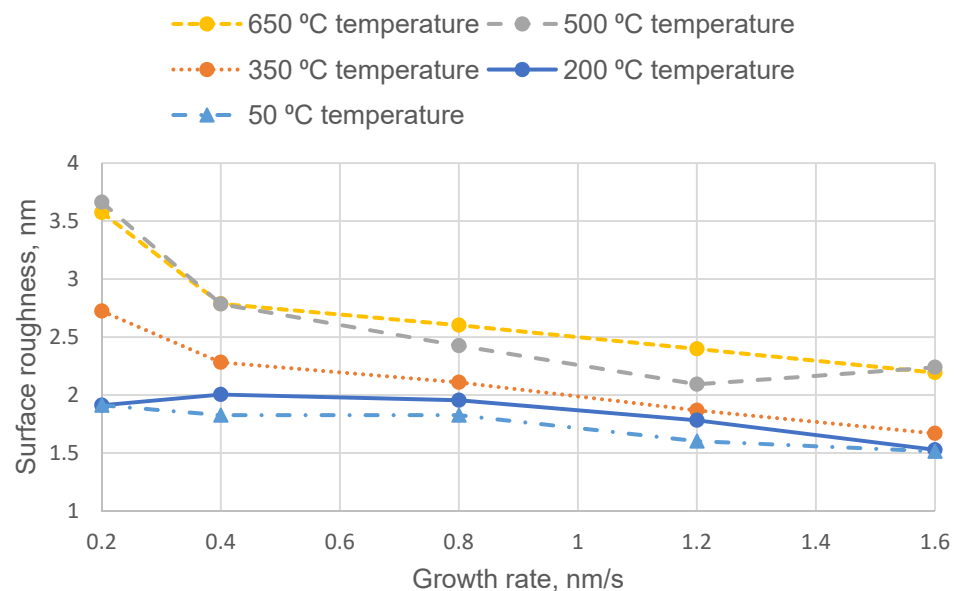


**Figure 11.** Plots of surface roughness versus growth rate obtained by using different substrate temperatures.

To understand reasons for the given relationship between the surface roughness and the growth rate, the plots of average grain size (of component A) versus growth rate were obtained at the substrate temperatures of 350 and 650 °C (Figure 12). It is seen that the average grain size decreases monotonically as the growth rate increases at both substrate temperatures given, therefore both decreases in the surface roughness and the average grain size can be related. Hence, the monotonic decrease in the surface roughness caused by the increase in the growth rate can be attributed to the monotonic decrease in the average grain size under the given conditions. By comparing Figures 7 and 8 to Figures 11 and 12, it can be seen that the influence of the increase in the growth rate on the surface roughness (and on the average grain size) is opposite in comparison to the influence in the increase of the substrate temperature.

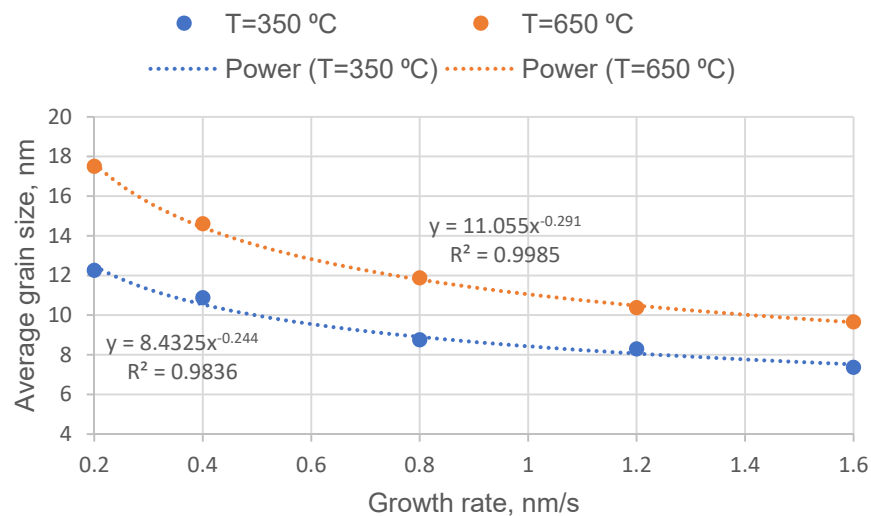


**Figure 12.** Plots of average grain size versus growth rate observed at the substrate temperatures of 350 °C and 650 °C.

#### 4. Conclusions

This study set out to gain a better understanding of the influence of substrate temperature and growth rate on the surface roughness and the phase structure of thin films and explore these relationships experimentally and by using a mathematical model.

It was determined that a different microstructure with different surface morphologies is obtained depending on the temperature of the substrate. At substrate temperatures below 300 °C, thin films are comprised of small grains having ~8 nm height and ~200 nm width grains, whereas large triangle prism shape grains are predominant while using substrates above 300 °C.

The modeling results revealed that the increase in the substrate temperature resulted in the monotonic increase in the surface roughness of thin films in most cases. A similar relationship was noticed between the size of nanoparticles formed and the substrate temperature. Moreover, the nonlinear relationships between surface roughness and the average size of nanoparticles were also discovered, so the increase in the surface roughness with an increase of temperature was influenced by the increase of nanoparticle size. Modeling results also showed that the increase in the growth rate caused the monotonic decrease in the surface roughness of thin films in most cases. The decrease in the surface roughness in the given condition was also attributed to the decrease in the average size of nanoparticles.

**Supplementary Materials:** The following are available online at <https://www.mdpi.com/article/10.3390/coatings12010031/s1>, Table S1: EDS analysis results of ScAlSZ thin films, (vd—deposition rate, Td—substrate temperature during deposition, and c—atomic concentration of elements).

**Author Contributions:** Conceptualization, A.G., G.L., G.K. and M.S.; methodology, A.G., G.L., G.K. and M.S.; software, G.K.; validation, G.K., A.G., M.G. and T.M.; investigation, G.L., M.S., K.B., and D.V.; computer modeling, A.G., G.K., M.G. and T.M.; writing—original draft preparation, M.S. (introduction, experimental, AFM and SEM results), G.K. and A.G. (introduction, kinetic model, results of computer modeling, conclusions); writing—review and editing, A.G., M.S., G.K., G.L., K.B. and M.G.; visualization, G.K. and M.S.; supervision and funding acquisition, A.G. and G.L. All authors have read and agreed to the published version of the manuscript.

**Funding:** This project has received funding from European Regional Development Fund (project No 01.2.2-LMT-K-718-01-0071) under grant agreement with the Research Council of Lithuania (LMTLT).

**Institutional Review Board Statement:** Not applicable.

**Informed Consent Statement:** Not applicable.

**Data Availability Statement:** Not applicable.

**Conflicts of Interest:** The authors declare no conflict of interest.

## References

1. Kawada, T.; Mizusaki, J. Current electrolytes and catalysts. In *Handbook of Fuel Cells*; Vielstich, W.H., Gasteiger, A.H., Yokokawa, A.L., Eds.; John Wiley & Sons: Hoboken, NJ, USA, 2010.
2. Talebi, T.; Haji, M.; Raissi, B. Effect of sintering temperature on the microstructure, roughness and electrochemical impedance of electrophoretically deposited YSZ electrolyte for SOFCs. *Int. J. Hydrogen Energy* **2010**, *35*, 9420–9426. [[CrossRef](#)]
3. Chen, X.J.; Khor, K.A.; Chan, S.H.; Yu, L.G. Influence of microstructure on the ionic conductivity of yttria-stabilized zirconia electrolyte. *Mater. Sci. Eng. A* **2002**, *335*, 246–252. [[CrossRef](#)]
4. Gibson, I.R.; Dransfield, G.P.; Irvine, J.T.S. Sinterability of commercial 8 mol% yttria-stabilized zirconia powders and the effect of sintered density on the ionic conductivity. *J. Mater. Sci.* **1998**, *33*, 4297–4305. [[CrossRef](#)]
5. Guo, X.; Maier, J. Grain Boundary Blocking Effect in Zirconia: A Schottky Barrier Analysis. *J. Electrochem. Soc.* **2002**, *148*, E121. [[CrossRef](#)]
6. Zhang, L.; Virkar, A.V. On Space Charge and Spatial Distribution of Defects in Yttria-Stabilized Zirconia. *J. Electrochem. Soc.* **2017**, *164*, F1506–F1523. [[CrossRef](#)]
7. Maier, J. On the Conductivity of Polycrystalline Materials. *Ber. Bunsenges. Phys. Chem.* **1986**, *90*, 26–33. [[CrossRef](#)]
8. Göbel, M.C.; Gregori, G.; Maier, J. Mixed conductivity in nanocrystalline highly acceptor doped cerium oxide thin films under oxidizing conditions. In *Physical Chemistry Chemical Physics*; Royal Society of Chemistry: London, UK, 2011; Volume 13, pp. 10940–10945.
9. Kim, S.; Avila-Paredes, H.J.; Wang, S.; Chen, C.T.; De Souza, R.A.; Martin, M.; Munir, Z.A. On the conduction pathway for protons in nanocrystalline yttria-stabilized zirconia. *Phys. Chem. Chem. Phys.* **2009**, *11*, 3035–3038. [[CrossRef](#)] [[PubMed](#)]
10. Durá, O.J.; López De La Torre, M.A.; Vázquez, L.; Chaboy, J.; Boada, R.; Rivera-Calzada, A.; Santamaria, J.; Leon, C. Ionic conductivity of nanocrystalline yttria-stabilized zirconia: Grain boundary and size effects. *Phys. Rev. B-Cond. Matter Mater. Phys.* **2010**, *81*, 184301. [[CrossRef](#)]
11. Fleig, J. A Finite Element Study on the Grain Boundary Impedance of Different Microstructures. *J. Electrochem. Soc.* **2006**, *145*, 2081. [[CrossRef](#)]
12. Aoki, M.; Chiang, Y.M.; Kosacki, I.; Lee, L.J.R.; Tuller, H.; Liu, Y. Solute segregation and grain-boundary impedance in high-purity stabilized zirconia. *J. Am. Ceram. Soc.* **1996**, *79*, 1169–1180. [[CrossRef](#)]
13. Kosacki, I.; Suzuki, T.; Petrovsky, V.; Anderson, H.U. Electrical conductivity of nanocrystalline ceria and zirconia thin films. *Solid State Ion.* **2000**, *136–137*, 1225–1233. [[CrossRef](#)]
14. Kiguchi, T.; Kodama, Y.; Konno, T.J.; Funakubo, H.; Sakurai, O.; Shinozaki, K. Chemical and structural effects on ionic conductivity at columnar grain boundaries in yttria-stabilized zirconia thin films. *J. Ceram. Soc. Jpn.* **2014**, *122*, 430–435. [[CrossRef](#)]
15. Kiguchi, T.; Konno, T.J.; Funakubo, H.; Sakurai, O.; Shinozaki, K. Columnar grain boundary coherence in yttria-stabilized zirconia thin film: Effects on ionic conductivity. *J. Ceram. Soc. Jpn.* **2014**, *122*, 72–77. [[CrossRef](#)]
16. Boch, P.; Nièpce, J.-C.; Carter, C.B.; Norton, M.G.; Caruta, B.M. *Ceramics and Composite Materials*; Springer: New York, NY, USA, 2007.
17. Nagarajan, G. Thermodynamic Properties of Some Metal Hexafluorides. *Bull. Des. Soc. Chim. Belges* **2010**, *71*, 77–81. [[CrossRef](#)]
18. Petrov, I.; Barna, P.B.; Hultman, L.; Greene, J.E. Microstructural evolution during film growth. *J. Vac. Sci. Technol. A Vac. Surf. Films* **2003**, *21*, S117–S128. [[CrossRef](#)]
19. Barna, P.B.; Adamik, M. Fundamental structure forming phenomena of polycrystalline films and the structure zone models. *Thin Solid Films* **1998**, *317*, 27–33. [[CrossRef](#)]
20. Greene, J.E. Thin Film Nucleation, Growth, and Microstructural Evolution: An Atomic Scale View. In *Handbook of Deposition Technologies for Films and Coatings*; Elsevier Science: Amsterdam, The Netherlands, 2013; Volume 53, pp. 554–620. ISBN 9788578110796.
21. Muzard, S.; Templier, C.; Delafond, J.; Girard, J.C.; Thiaudiere, D.; Pranevicius, L.; Galdikas, A. Development of the micro structure of sputter deposited gold on amorphous carbon. *Surf. Coat. Technol.* **1998**, *100–101*, 98–102. [[CrossRef](#)]
22. Evans, J.W.; Thiel, P.A.; Bartelt, M.C. Morphological evolution during epitaxial thin film growth: Formation of 2D islands and 3D mounds. *Surf. Sci. Rep.* **2006**, *61*, 1–128. [[CrossRef](#)]
23. Galdikas, A.; Čerapaite-Trušinskiene, R.; Laukaitis, G.; Dudonis, J. Real-time kinetic modeling of YSZ thin film roughness deposited by e-beam evaporation technique. *Appl. Surf. Sci.* **2008**, *255*, 1929–1933. [[CrossRef](#)]
24. Metiu, H.; Lu, Y.-T.; Zhang, Z. Epitaxial growth and the art of computer simulations. *Science* **1992**, *255*, 1088–1092. [[CrossRef](#)] [[PubMed](#)]
25. Galdikas, A. Non-monotonous dependence of surface roughness on factors influencing energy of adatoms during thin island film growth. *Surf. Sci.* **2006**, *600*, 2705–2710. [[CrossRef](#)]
26. Kaiser, N. Review of the fundamentals of thin-film growth. *Appl. Opt.* **2002**, *41*, 3053. [[CrossRef](#)]
27. Barna, P.B.; Adamik, M. Growth Mechanisms of Polycrystalline Thin Films. In *Science and Technology of Thin Films*; Maticotta, F.C., Ottaviani, G., Eds.; World Scientific Publishing: Singapore, 1995; pp. 1–28.
28. Knuyt, G.; Quaeys, C.; D’Haen, J.; Stals, L.M. A quantitative model for the evolution from random orientation to a unique texture in PVD thin film growth. *Thin Solid Films* **1995**, *258*, 159–169. [[CrossRef](#)]

29. Kairaitis, G.; Grigaliūnas, A.; Baginskas, A.; Galdikas, A. Kinetic modeling of phase separation and surface segregation in growing a-C:Ni thin films. *Surf. Coat. Technol.* **2018**, *352*, 120–127. [[CrossRef](#)]
30. Kurc, B.; Pigłowska, M.; Rymaniak, Ł.; Fuć, P. Modern nanocomposites and hybrids as electrode materials used in energy carriers. *Nanomaterials* **2021**, *11*, 538. [[CrossRef](#)]
31. Calderon Velasco, S.; Cavaleiro, A.; Carvalho, S. Functional properties of ceramic-Ag nanocomposite coatings produced by magnetron sputtering. *Prog. Mater. Sci.* **2016**, *84*, 158–191. [[CrossRef](#)]
32. Armelao, L.; Barreca, D.; Bottaro, G.; Gasparotto, A.; Gross, S.; Maragno, C.; Tondello, E. Recent trends on nanocomposites based on Cu, Ag and Au clusters: A closer look. *Coord. Chem. Rev.* **2006**, *250*, 1294–1314. [[CrossRef](#)]
33. Charton, C.; Fahland, M. Optical properties of thin Ag films deposited by magnetron sputtering. *Surf. Coat. Technol.* **2003**, 174–175, 181–186. [[CrossRef](#)]
34. Tamulevičius, S.; Meškinius, Š.; Tamulevičius, T.; Rubahn, H.G. Diamond like carbon nanocomposites with embedded metallic nanoparticles. *Rep. Prog. Phys.* **2018**, *81*, 024501. [[CrossRef](#)]
35. Derby, B.; Cui, Y.; Baldwin, J.K.; Misra, A. Effects of substrate temperature and deposition rate on the phase separated morphology of co-sputtered, Cu-Mo thin films. *Thin Solid Films* **2018**, *647*, 50–56. [[CrossRef](#)]
36. Ankit, K.; Derby, B.; Raghavan, R.; Misra, A.; Demkowicz, M.J. 3-D phase-field simulations of self-organized composite morphologies in physical vapor deposited phase-separating binary alloys. *J. Appl. Phys.* **2019**, *126*, 075306. [[CrossRef](#)]
37. Bouaouina, B.; Mastail, C.; Besnard, A.; Mareus, R.; Nita, F.; Michel, A.; Abadias, G. Nanocolumnar TiN thin film growth by oblique angle sputter-deposition: Experiments vs. simulations. *Mater. Des.* **2018**, *160*, 338–349. [[CrossRef](#)]
38. To, T.B.T.; Aarão Reis, F.D.A. Domain formation in the deposition of thin films of two-component mixtures. *J. Alloys Compd.* **2020**, *835*, 155093. [[CrossRef](#)]
39. Mińkowski, M.; Załuska-Kotur, M.A.; Kret, S.; Chusnutdinow, S.; Schreyeck, S.; Brunner, K.; Molenkamp, L.W.; Karczewski, G. Self-organization process in crystalline PbTe/CdTe multilayer structures: Experiment and Monte Carlo simulations. *J. Alloys Compd.* **2018**, *747*, 809–814. [[CrossRef](#)]
40. Zhou, X.; Yu, X.; Jacobson, D.; Thompson, G.B. A molecular dynamics study on stress generation during thin film growth. *Appl. Surf. Sci.* **2019**, *469*, 537–552. [[CrossRef](#)]
41. Stewart, J.A.; Dingreville, R. Microstructure morphology and concentration modulation of nanocomposite thin-films during simulated physical vapor deposition. *Acta Mater.* **2020**, *188*, 181–191. [[CrossRef](#)]
42. Powers, M.; Derby, B.; Nerlige Manjunath, S.; Misra, A. Hierarchical morphologies in co-sputter deposited thin films. *Phys. Rev. Mater.* **2020**, *4*, 123801. [[CrossRef](#)]
43. Kairaitis, G.; Galdikas, A. Modelling of phase structure and surface morphology evolution during compound thin film deposition. *Coatings* **2020**, *10*, 1077. [[CrossRef](#)]
44. Singh, A.V.; Ferri, M.; Tamplenizza, M.; Borghi, F.; Divitini, G.; Ducati, C.; Lenardi, C.; Piazzoni, C.; Merlini, M.; Podestà, A.; et al. Bottom-up engineering of the surface roughness of nanostructured cubic zirconia to control cell adhesion. *Nanotechnology* **2012**, *23*, 475101. [[CrossRef](#)]
45. Heiroth, S.; Lippert, T.; Wokaun, A.; Döbeli, M. Microstructure and electrical conductivity of YSZ thin films prepared by pulsed laser deposition. *Appl. Phys. A* **2008**, *93*, 639–643. [[CrossRef](#)]
46. Eftekhari, L.; Raoufi, D. Crystallography characteristics of tetragonal nano-zirconia films under various oxygen partial pressure. *Surf. Eng.* **2018**, *35*, 618–626. [[CrossRef](#)]
47. Sriubas, M.; Kainbayev, N.; Virbukas, D.; Bočkute, K.; Rutkuniene, Ž.; Laukaitis, G. Structure and Conductivity Studies of Scandia and Alumina Doped Zirconia Thin Films. *Coatings* **2019**, *9*, 317. [[CrossRef](#)]
48. Rivière, J.P.; Pichon, L.; Drouet, M.; Poquillon, D.; Galdikas, A. Silicon based coatings deposited by dynamic ion mixing for oxidation protection of a Ti6242 alloy. *Surf. Coat. Technol.* **2007**, *201*, 8343–8347. [[CrossRef](#)]
49. Pandey, S.K.; Thakur, O.P.; Raman, R.; Goyal, A.; Gupta, A. Structural and optical properties of YSZ thin films grown by PLD technique. *Appl. Surf. Sci.* **2011**, *257*, 6833–6836. [[CrossRef](#)]
50. Zoita, N.C.; Grigorescu, C.E.A. Influence of growth temperature and deposition duration on the structure, surface morphology and optical properties of InN/YSZ (1 0 0). *Appl. Surf. Sci.* **2012**, *258*, 6046–6051. [[CrossRef](#)]